TU Delft

Delft University of Technology

Document Version
Final published version

Licence
CC BY

Citation (APA)
Aghajanloo, M., Taghinejad, S. M., Zaynetdinov, T., Jones, S., Voskov, D., & Farajzadeh, R. (2026). CO2 hydrate saturation, permeability and injectivity in the saline environments: Effect of mean ionic activity. *Journal of CO2 Utilization*, *106*, Article 103380. https://doi.org/10.1016/j.jcou.2026.103380

Important note
To cite this publication, please use the final published version (if applicable).
Please check the document version above.

Copyright
In case the licence states “Dutch Copyright Act (Article 25fa)”, this publication was made available Green Open Access via the TU Delft Institutional Repository pursuant to Dutch Copyright Act (Article 25fa, the Taverne amendment). This provision does not affect copyright ownership.
Unless copyright is transferred by contract or statute, it remains with the copyright holder.

Sharing and reuse
Other than for strictly personal use, it is not permitted to download, forward or distribute the text or part of it, without the consent of the author(s) and/or copyright holder(s), unless the work is under an open content license such as Creative Commons.

Takedown policy
Please contact us and provide details if you believe this document breaches copyrights.
We will remove access to the work immediately and investigate your claim.

This work is downloaded from Delft University of Technology.

Journal of CO2 Utilization 106 (2026) 103380

Contents lists available at ScienceDirect

Journal of CO2 Utilization

journal homepage: www.elsevier.com/locate/jcou

CO_2 hydrate saturation, permeability and injectivity in the saline environments: Effect of mean ionic activity

M. Aghajanloo [a,*], S.M. Taghinejad [a], T. Zaynetdinov [c], S. Jones [a], D. Voskov [a,b], R. Farajzadeh [a,c]

[a] Delft University of Technology, Department of Geoscience and Engineering, Stevinweg 1, Delft 2628 CN, the Netherlands
[b] Department of Energy Science and Engineering, Stanford University, 367 Panama street, CA 94305, United States
[c] Shell Global Solutions International B.V., Grasweg 31, Amsterdam 1031 HW, the Netherlands

ARTICLE INFO

Keywords:
CO_2 Storage
Depleted Gas Reservoirs
CO_2 Hydrate
Salinity
Mean Ionic Activity
Permittivity
Permeability Impairment
CO_2 Injectivity

ABSTRACT

In depleted or low-pressure subsurface reservoirs, the formation of CO_2 hydrate at low temperatures, induced by vaporization and isenthalpic expansion during dense CO_2 injection, can significantly impair well injectivity. The formation of CO_2 hydrates is governed by multiple factors, including CO_2 availability and its solubility, the properties of the surrounding fluids, and the characteristics of the rock. A key parameter influencing water activity and CO_2 solubility is the salinity of in-situ brine, which affects both the thermodynamics and kinetics of hydrate formation. The impact of salinity varies with the type and concentration of dissolved salts. This study investigates the impacts of two prevalent formation water salts, NaCl and $CaCl_2$ on CO_2 hydrate induction time, hydrate saturation, rock permeability reduction, and their implications for CO_2 injectivity. Coreflood experiments were performed under dynamic flow conditions, supplemented by computed tomography (CT) scanning to provide in-situ saturation profiles. The primary aim is to establish a correlation between the aforementioned parameters and mean ionic activity, thereby facilitating a generalized application of the results irrespective of the specific salt type. Empirical results indicate a marginally extended induction period at elevated initial salinity levels. Furthermore, an increase in mean ionic activity correlates with a decrease in hydrate saturation, which consequently leads to less significant reductions in permeability and injectivity.

1. Introduction

The rapid increase in CO_2 emissions resulting from anthropogenic sources presents significant environmental risks, with global warming being the most urgent concern [1,2]. Carbon capture and storage (CCS) is widely acknowledged as an essential strategy for mitigating global CO_2 emissions. Nevertheless, the effectiveness of CCS as a large-scale mitigation strategy is not universally agreed upon, due to uncertainties in long-term containment, affordability, and deployment rate [3]. Depleted hydrocarbon reservoirs stand out as highly promising options for CO_2 storage [4-7]. However, in low-pressure reservoirs, introducing CO_2 injection can lead to low temperatures as a result of Joule-Thomson cooling (JTC) effect due to considerable pressure gradients. The possibility of CO_2 hydrate formation under these conditions is a significant concern, as it can result in severe permeability reduction and consequently injectivity loss [8]. This impact is dependent on the initial water saturation, the extent of water-to-hydrate conversion, and hydrate saturation [9].

The amount of water converting to hydrate and CO_2 hydrate saturation are affected by various factors including CO_2 availability/deficiency [10,11], fluid composition (e.g. salts, contaminants, and gaseous impurities) [12,13], and rock characteristics such as pore geometry, porosity, permeability, and wettability [14-16]. Studies have demonstrated that among these factors, the salt content of in-situ brine is a key determinant in hydrate nucleation since salts act as thermodynamic hydrate inhibitors (THIs) and depress the hydrate formation temperature at a given pressure [17]. Nevertheless, the extent of this effect is influenced by the type and concentration of salt. Salts have an inhibition mechanism that differs from alcohols or glycols. They ionize in solution and interact with water molecules through strong Coulombic forces (long-range interactions), that are significantly stronger than hydrogen bonding or van der Waals forces, which drive clustering around apolar solute molecules. This interaction decreases the chemical potential of the water, which can enhance its stability as a liquid water rather than allowing water to form hydrates, particularly at high ion concentrations [12,18]. This robust interaction between salt ions and water molecules also reduces the solubility of gas molecules in the aqueous phase, which

* Corresponding author.
E-mail address: M.Aghajanloo@tudelft.nl (M. Aghajanloo).

https://doi.org/10.1016/j.jcou.2026.103380
Received 1 April 2025; Received in revised form 9 February 2026; Accepted 27 February 2026
Available online 5 March 2026
2212-9820/© 2026 The Authors. Published by Elsevier Ltd. This is an open access article under the CC BY license (http://creativecommons.org/licenses/by/4.0/).

Nomenclature

Acronym

$\gamma_{\pm}$	mean ionic activity coefficient
$a_{i_{\pm}}$	mean ionic activity
$a_{i_{\pm}}{}'$	modified mean ionic activity
a_{+}	cation parameter of permittivity
a_{-}	onion parameter of permittivity
A	Debye–Hückel numerical constant
A_{φ}	Debye–Hückel slope
B	Debye–Hückel numerical constant
b^{γ}_{MX}	Pitzer binary interaction coefficient
BPR	Back Pressure Regulator
c_{+}	concentration of cation charges in permittivity
c_{-}	concentration of onion charges in permittivity
c^{γ}_{MX}	Pitzer ternary interaction coefficient
CCS	Carbon Capture and Storage
CPA	Cubic Plus Association
CT	Computed tomography
DP	Differential Pressure
EoS	Equation of State
I	ionic strength
II	Injectivity Index
IPCC	Intergovernmental Panel on Climate Change
JTC	Joule-Thomson Cooling
k	permeability
MFC	Mass Flow Controller
$m_{\pm}$	mean molality
P	Pressure Transducer
PV	Pore Volume
Q_{CO2}	injection rate
SRCCS	Special Report on CCS
S_H	hydrate saturation
S_w	water saturation
T	Temperature
TC	Thermocouple
THIs	Thermodynamic Hydrate Inhibitors
XRD	X-Ray Diffraction
z	ions charge in solution

Subscript & Superscript

H	hydrate
eq	equilibrium
exp	experimental
sub	subcooling
w	water

Greek Character

ΔP	pressure difference
ϕ	osmotic coefficient
ν_{+}	stoichiometric coefficient
ε_r	static permittivity
$\varepsilon_{S,0}$	relative permittivity of pure saturated liquid water

is required for hydrate nucleation, commonly termed salting out. The clustering of ions and the salting out effect together result in a lower hydrate formation temperature (higher degree of subcooling) [17]. However, the effects of different ions on hydrate kinetics are known to vary [19]. Therefore, the impact of salt on gas hydrate nucleation time and final cluster growth can be discussed for the dynamic system in terms of salt type (i.e. monovalent or divalent) and concentration. Regarding concentration, not only does the initial concentration of salts depress hydrate equilibrium temperature, but a salinity gradient is created during hydrate nucleation process, as salts do not incorporate into the hydrate lattice [20,21]. This gradient leads to an increase in mean ionic activity around the nucleation zone, which may limit further hydrate nucleation under the given thermodynamic conditions [12,22, 17]. The ion size and charge density play crucial roles in organizing water molecules, a phenomenon known as water-ordering [23]. Smaller ions with greater charge density, like Na^+ , promote water-ordering, while the existence of the anion Cl^- can lead to water-disordering [24-26]. Therefore, anions have a greater influence than cations on gas hydrate stability in electrolyte solutions [27].

Empirical investigations on the permeability of hydrate-bearing sediments, combined with dynamic flow experiments as a widely applied method, aim to determine relative permeability and assess the resulting CO_2 injectivity. CO_2 injectivity is defined as the rate at which CO_2 can be introduced into a geological formation under a given pressure gradient, particularly in the presence of electrolyte solutions. The majority of existing studies has mainly concentrated on the effect of salts on various properties of gas hydrates in bulk systems, while very few studies have investigated CO_2 hydrate behavior in porous rocks [28,29]. Husebø et al. Husebø et al., [12] measured methane consumption in porous rocks and demonstrated that consumption during hydrate generation is predominantly influenced by total brine salinity. In their conclusions, they highlighted that salinities below seawater levels have minimal effect on the fraction of methane consumed during hydrate formation in porous media, whereas a significant decrease in gas consumption occurs when salinity exceeds seawater levels. Another study [21] found that salt ions in seawater slightly decrease the water conversion to hydrate in porous media without affecting the hydrate kinetics. However, these studies demonstrate that hydrate characteristics are specific to the type of salt, constraining the applicability of the findings to other conditions. Almenningen et al. Almenningen et al., [30] employed high-pressure silicon-wafer micromodels, designed to replicate the characteristics of actual sandstone grains, to investigate methane hydrate decomposition behaviors due to the depressurization and thermal stimulation as influenced by salt concentration (0–5 wt% NaCl). Their findings revealed a significant connection between the initial distribution of methane hydrates and their dissociation patterns. Additionally, hydrate re-nucleation was detected during dissociation, attributed to local salinity gradients.

The objective of present study is to investigate the kinetics of CO_2 hydrate in a porous medium partially filled with saline brines under flowing conditions and to quantify the impact of salinity (type and concentration) on the permeability reduction. This research uses the mean ionic activity as a key parameter. Consequently, this paper is structured into three main parts. The experimental phase comprises core flooding tests conducted on Berea sandstone core plugs under a constant degree of subcooling, defined by the equilibrium temperature depression in the presence of NaCl and $CaCl_2$ ions—the predominant salts in oil and gas reservoirs—at concentrations ranging from 1 to 25 wt%. These experiments were carried out under a medical CT scanner to quantify phase saturations. The second part of the paper focuses on modeling the ionic activity coefficient using Debye-Hückel and Pitzer models to derive the mean ionic activity of the tested solutions. The final section establishes hydrate saturation as functions of the mean ionic activity and permittivity. This analysis is based on the extent of rock pore blockage by solid CO_2 hydrate.

In this work, we investigate NaCl (monovalent) and $CaCl_2$ (divalent) because they are among the most abundant salts in formation waters of depleted gas reservoirs and they capture distinct effects of ion valency on CO_2 hydrate thermodynamics and kinetics. To ensure our findings are broadly applicable rather than specific to a given salt, we interpret the

results in terms of mean ionic activity, which consolidates both salt type and concentration into a single physicochemical descriptor. Although all experiments were conducted using Berea sandstone (mineralogy shown in Table 2) to isolate salinity effects, we acknowledge that reservoir mineral composition and other in-situ conditions, such as gas impurities, may also influence hydrate formation [29].

Prior to the interpretation of the results, it is important to define some key terminology. Induction time refers to the onset of macroscopic hydrate nucleation, identified when sufficient CO_2 is incorporated into the hydrate lattice to produce a detectable sign, and confirmed by a transient temperature rise due to the exothermic nature of hydrate formation. In this study, induction time is measured from the start of CO_2 injection under isothermal conditions to the first occurrence of CO_2 hydrate signatures. Subcooling is defined as the temperature difference from the reference condition, usually indicating the deviation from the equilibrium state. Depression temperature refers to the equilibrium temperature reduction under constant pressure from the reference condition due to presence of salt.

2. Experimental method and materials

2.1. Material

The specifications for the materials used in the experiments are outlined in Table 1. All tests were conducted using Berea sandstone, an outcrop from the Berea quarry in Ohio, USA. The mineralogy measured via X-ray diffraction (XRD) analysis, is reported in Table 2. It has a measured porosity of 21% and an absolute permeability ranging from 200 to 300 mD and pore radius on the order of 10–100 μm. The core plug used in the experiments was 3.8 cm in diameter with 17 cm in length with calculated pore volume (PV) of 38.5 ml.

Experiments were designed for two-phase core flooding, utilizing an X-ray CT scanner (Siemens Somatom Volume) to monitor the phase behavior of CO_2, brine, and hydrate throughout the experimental process. This includes brine saturation, hydrate nucleation, and growth stages, as depicted in Fig. 1.

The setup features a polyetheretherketone (PEEK) core holder containing a Berea core coated with epoxy resin to form a protective layer that shields the fluids. A jacket surrounds the core holder, through which a cooling medium is circulated by means of a circulator (LAUDA Proline RP845). Pressure transducers (GE UNIK 5000— Accuracy to ±0.04% Full Scale, ranges from 0.07 to 80 bar) measure absolute pressure at four points. Two differential pressures (Endress and Hauser, Deltabar S, ranges: −0.3 to +0.3 bar) monitor the pressure differences from the inlet to the middle, and from the middle to the outlet. Thermocouples are positioned at the inlet and on the core surface to record localized temperature variations. A regulated back pressure is connected to an N_2 cylinder, adjusting and maintaining system pressure. The data from the thermocouple and pressure transducer are recorded via the data acquisition box. The fluid control system comprises a pulse-free piston pump (Quizix QX-6000HC) for driving solutions through the core and a gas mass flow controller (Bronkhorst F-230M) to regulate the gas flow rate.

Table 1
Specification of the materials utilized in this work.

Component	chemical formula	Manufacturer	Purity
Carbon dioxide[a]	CO_2	Linde gas	≥ 99.7%.
Nitrogen[a]	N_2	Linde gas	≥ 99.999%
Sodium Chloride	NaCl	Fisher scientific	≥ 99.5%
Calcium Chloride Dihydrate	$CaCl_2.2H_2O$	Thermo scientific	≥ 99%
Demineralized Water	H_2O	TUDelft water lab	

[a] CO_2 and N_2 were 10 L bottle with pressure of 200 bar

Table 2
XRD analysis of crushed Berea sandstone powder, from the sample used for the experiments.

Compound	Mineral Name	Chemical Formula	Quantity (wt %)
Silicon Oxide	Quartz	SiO_2	85
Aluminium Silicate Hydroxide	Kaolinite-1A	$Al_2(Si_2O_5)(OH)_4$	5
Sodium Aluminum Silicate	Albite	$NaAlSi_3O_8$	6
Potassium Aluminium Silicate	Microcline	$KAlSi_3O_8$	4

2.2. Experimental procedure

The experimental methodology is based on the core flooding test outlined in previous studies to measure CO_2 hydrate parameters applying isothermal methods in a partially saturated core [8]. Briefly, brine and N_2 were co-injected into the horizontal sandstone core to achieve the desired water saturation and uniform brine distribution along the core [31]. N_2 was selected as the saturation gas phase because it has low solubility in brine and a negligible tendency to form hydrates under the experimental pressure–temperature conditions. This avoids premature hydrate formation during the subsequent cooling stage, which could occur if dissolved CO_2 were present in the aqueous phase during the cooling process. In this approach, the gas fractional flow (f_g) is maintained significantly higher than the liquid fractional flow (f_l), ensuring that the liquid phase spreads throughout the core pores. if any non-uniform distribution is observed (assessed via CT scans), N_2 injection continued at elevated temperature to promote more uniform brine distribution along the core. This procedure was validated with a ± 0.5% error margin due to dead volume of the system, which included the inlet/outlet lines and core holder caps. Following this, residual brine was retracted from the injection line, while N_2 injection at the same expected rate as CO_2 injection (1 ml/min) was maintained for several hours to dry the flow path and connections, as well as to establish baseline pressure corresponding to the CO_2 hydrate phase boundary. During this period, the temperature was set to a value with 6 ° of subcooling based on the depression temperature due to the brine salinity. The identical subcooling degree in all tests allows the assessment of hydrate behavior independent of the driving force. Subsequently, CO_2 injection was initiated in the gas phase at a constant mass rate under isothermal conditions. Considering the very low solubility of N_2 in water at low temperatures, it is expected that the continuous injection of CO_2 rapidly and effectively displaced the majority of the N_2, with any residual fraction exerting a negligible influence on the hydrate phase equilibrium at low pressures. The CO_2 injection was sustained until complete CO_2 hydrate growth was achieved, as indicated either via a stabilized pressure decline or by the development of a hydrate blockage that impeded further injection. Hydrate dissociation was then induced via thermal stimulation, by increasing the temperature of the core to 20°C for 12 hrs. To increase the accuracy of the results, given the stochastic nature of hydrate nucleation, the subsequent cycle of CO_2 hydrate formation was initiated after cooling the core to the experimental temperature under N_2 injection. Since hydrate formation in this study was conducted using an isothermal method, this approach ensured a consistent baseline across all cycles and improved the repeatability of the findings.

To determine the permeability of the sandstone core, a gas permeability test was carried out. The absolute permeability was quantified considering the Klinkenberg effect [32]. Furthermore, to assess any permeability change resulting from the hydrate formation and decomposition process, a brine permeability test was performed at the end of the test on the fully saturated core [33].

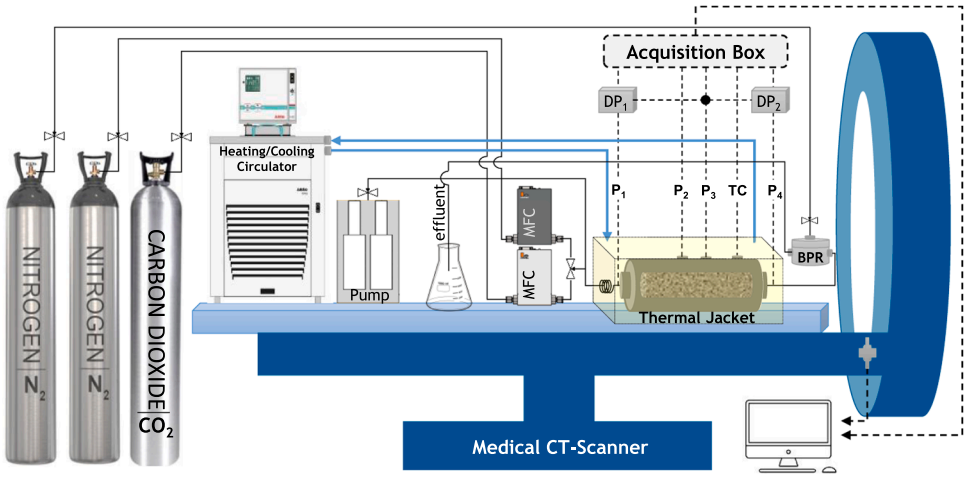

Fig. 1. Schematic of the laboratory equipment. (BPR) Back Pressure Regulator; (DP) Differential Pressure; (MFC) Mass Flow Controller; (P) Pressure Transducer; (TC) Thermocouple.

2.3. Experimental conditions

Considering that salts act as thermodynamic hydrate inhibitors by altering the activity of water molecules and shifting the hydrate stability conditions, understanding the relationship between hydrate equilibrium temperature depression and water activity is crucial. This relationship can help explain how salts stabilize water in the liquid phase rather than in the hydrate phase under given thermodynamic conditions. Therefore, to gain insight into the experimental conditions and create conditions conducive to hydrate formation in sandstone, the hydrate phase diagram was simulated utilizing HydraFLASH software employing the cubic plus association (CPA) equation of state (EoS) for aqueous phase and CO_2 (vapor and liquid). Fig. 2 shows the pressure-temperature [34] conditions of the seven experiments conducted in this study, categorized by different salinities. In addition, the condition for experiment 8 with a 25 wt% $CaCl_2$ solution is illustrated in Fig. 3, showing the test conditions using the step cooling method for hydrate formation. Fig. 2 and Fig. 3 illustrate that hydrate formation is most likely in the near-wellbore region, whereas farther into the reservoir the higher formation temperatures (despite elevated pressures) place the system outside the hydrate stability field, rendering hydrate formation unlikely. Additionally, in both figures, the dotted curve represents the CO_2 condensation line; its intersections with the solid curves for different salinities indicate the onset of CO_2 condensation under those brine conditions.

Nevertheless, the estimated depression temperature is based on bulk (capillarity-free) behavior; the influence of porous media on the CO_2–hydrate phase boundary must also be considered. This influence is not straightforward and depending on system conditions and pore-scale characteristics, porous media have been reported to both promote and inhibit hydrate formation [35]. Acting as a third interface, the solid matrix (rock) can organize interfacial water and alter capillary/thermodynamic conditions, thereby promoting hydrate formation thermodynamically and kinetically [36,37]. Porous media accelerate hydrate formation by modifying capillary and thermodynamic conditions and by providing heterogeneous nucleation sites. Interfacial ordering of water on pore surfaces facilitates clathrate cage assembly, enabling hydrate nucleation at higher temperatures and lower pressures than in bulk fluids [15,38]. Our investigation and experimental results

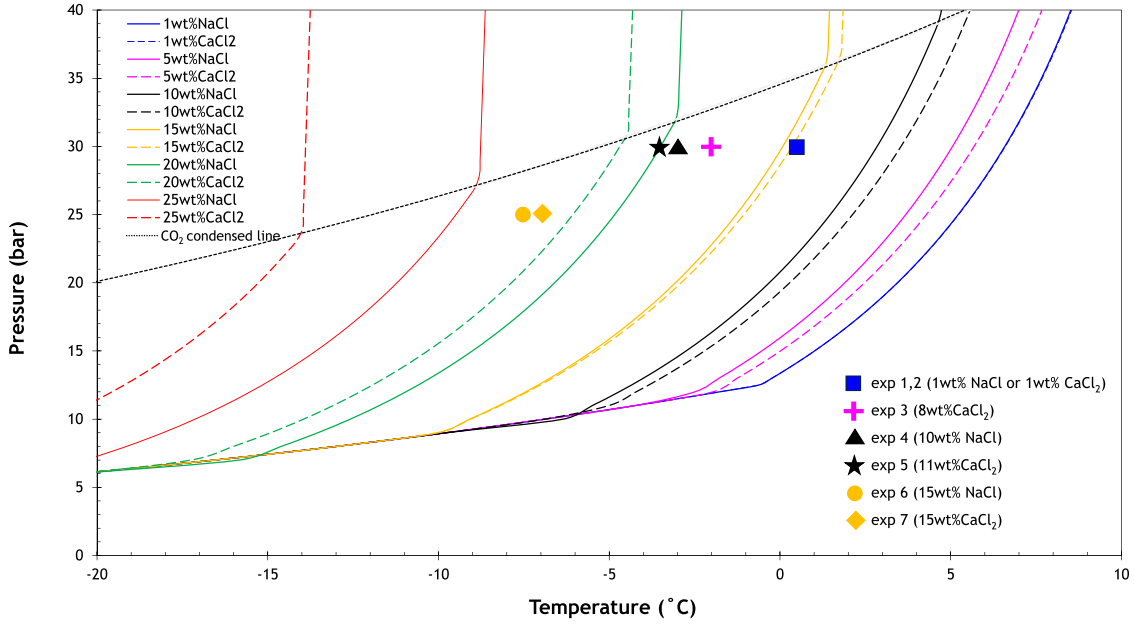

Fig. 2. CO_2 Hydrate equilibrium curves in presence of different NaCl/$CaCl_2$ solutions. The symbols represent the experimental conditions of the isothermal hydrate formation in the Berea core (exp 1–7).

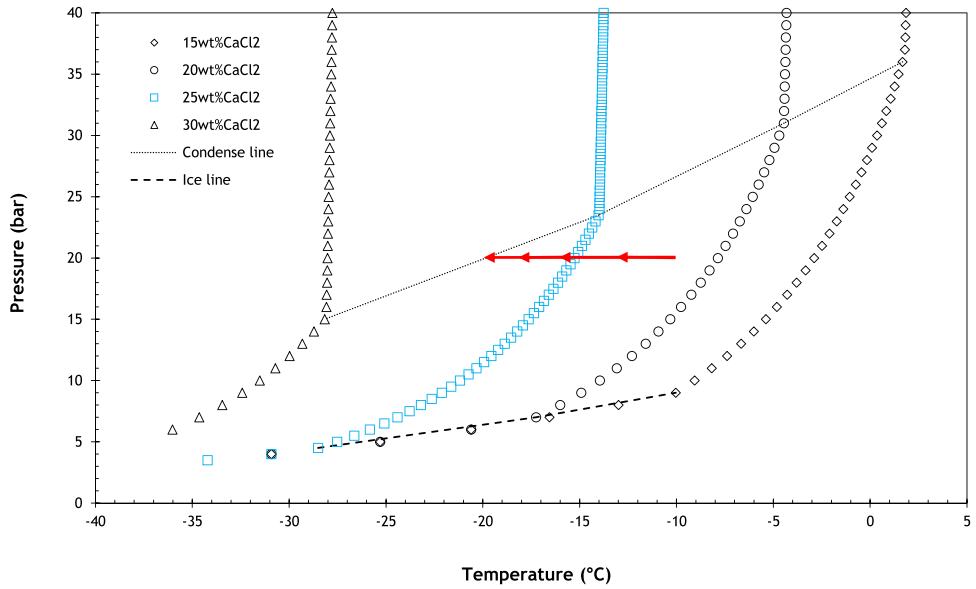

Fig. 3. CO_2 Hydrate depression temperature with different $CaCl_2$ solutions. The red arrows demonstrate the experimental conditions of hydrate formation by step cooling in the Berea core (exp 8).

also confirmed that the porous media can slightly displace the CO_2 hydrate phase boundary to higher temperatures [8]. The rock surface acts as a kinetic promoter by providing additional nucleation sites due to its large, rough surface, thereby accelerating and enhancing crystal growth [39]. Moreover, porous media exhibit good thermal conductivity, allowing it to dissipate the heat generated during hydrate formation efficiently, which promotes nucleation, particularly under low-pressure conditions where rapid heat generation occurs during hydration [40].

Table 3 provides detailed information on the water saturation levels throughout each experimental cycle, the degree of subcooling, as well as the measured gas and brine permeability before and after the test. A consistent subcooling degree (ΔT_{sub}) was maintained across all experiments to facilitate direct comparisons. The subcooling temperature is defined as $\Delta T_{sub} = T_{eq} - T_{exp}$, where T_{eq} represents the equilibrium temperature, and T_{exp} denotes the target experimental temperature for CO_2 hydrate formation based on the isothermal method.

3. Results and discussion

This section analyzes the pressure-temperature trajectory during CO_2 hydrate formation and dissociation cycles. To assess the hydrate-relevant parameters (e.g. induction time, hydrate saturation, and permeability reduction) independent of salt type, the mean ionic activity is defined based on the salinity ranges. The hydrate equilibrium pressure is then plotted against mean ionic activity at different temperatures. Subsequently, the induction time, which serves as a criterion for the onset of macroscopic hydrate nucleation, and hydrate saturation representing hydrate volume at the final growth stage, are assessed based on the mean ionic activity. Finally, normalized permeability and injectivity trends are discussed based on mean ionic activity.

Fig. 4 illustrates the measured pressure and temperature history over three CO_2 hydrate formation and dissociation cycles for a test with 43.5% brine saturation containing 1 wt% NaCl. The schematic on the left depicts the core holder and core sample, equipped with pressure

Table 3
Summary of experimental design.

Exp	Cycles	Initial Conditions: Brine+N_2 co-Injection			Permeability Test (mD)		
					Gas Permeability (Dry Core)	Brine Permeability (after CO_2 Injection)	
		Salinity (%)	Initial S_w (%)	ΔT_{sub} (°C)	whole core	1st Core Section[a]	2nd Core Section[b]
1	1st	1 wt% NaCl	43.5	6	150	124	112
	2nd		38.7				
	3rd		38.1				
2	1st	1 wt% $CaCl_2$	45.5	6	185	183	172
	2nd		45.4				
	3rd		43.8				
3	1st	8 wt% $CaCl_2$	30.5	6	130	124	126
	2nd		29.9				
4	1st	10 wt% NaCl	32.1	6	118	110	95
	2nd		32				
5	1st	11 wt% $CaCl_2$	34.4	6.5	112	96	83
	2nd		34.4				
6	1st	15 wt% NaCl	32.4	6	-	132	158
	2nd		32.4				
7	1st	15 wt% $CaCl_2$	35.0	6	-	136	163
	2nd		35.0				
8	-	25 wt% $CaCl_2$	35.7	Step cooling	243	223	214

[a] the section of core between P_1 and P_3 with the length of 10.5 cm
[b] the section of core P_3 and P_4 with the length of 6.5 cm

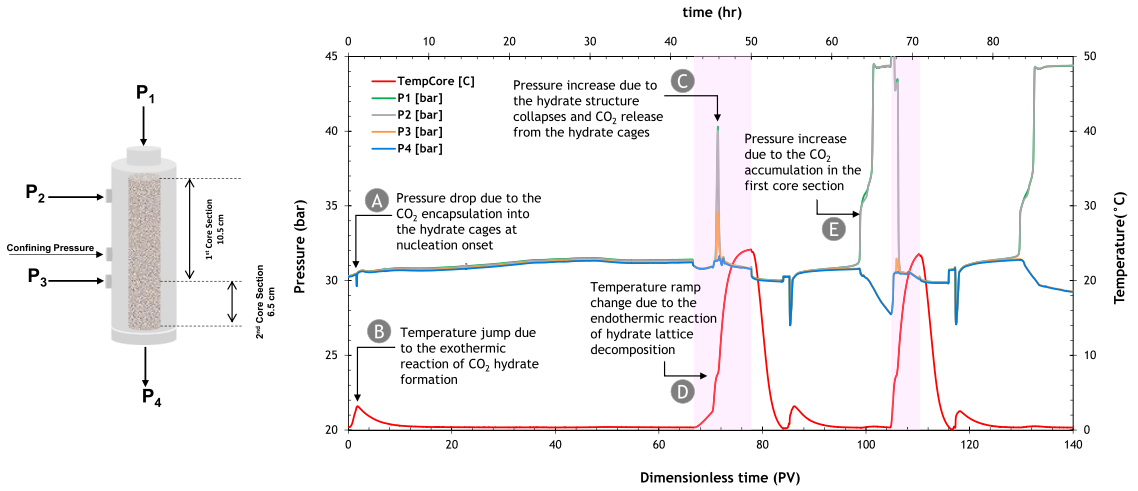

Fig. 4. The measured pressure and temperature history during CO_2 injection, hydrate generation, and decomposition for 43.5% water saturation with 1 wt% NaCl over three cycles. The initial conditions were set at 30 bar and 0.5°C. Pressure transducer is located at four points: the inlet (P_1), 2.25 cm from the inlet (P_2), 6.5 cm from the outlet (P_3), and the outlet (P_4). The shaded pink area indicates the hydrate dissociation step.

sensors and confining pressure monitoring points. The first core section corresponds to the inlet region, from P_1 to P_3, while the second section extends from P_3 to the outlet at P_4 (see Fig. 4). CO_2 injection commenced in the primary cycle after achieving the desired brine saturation and uniform distribution. The induction period, identified at the onset of macroscopic nucleation, was marked by a simultaneous pressure drop (A) and temperature rise (B). Once the hydrate nuclei stabilized, pressures gradually raised, reflecting the progress of hydrate clustering within the sandstone pores. Stabilization of PT conditions indicates the cessation of CO_2 hydrate growth. Nevertheless, volume expansion associated with hydrate formation can reduce rock porosity and potentially impair permeability in specific sections of the core. This can lead to complete blockage, as is particularly evident in the second and third cycles from P3 onward (E). Thermal stimulation at 24°C was employed to dissociate the hydrate structure. Upon hydrate lattice decomposition, a significant amount of trapped CO_2 was released, resulting in a temporary pressure increase (C) before excess CO_2 exited the core, considering the back pressure. A shift in the temperature ramp was also observed, attributed to the endothermic reaction of hydrate decomposition (D). In this specific case, following the dissociation of hydrate in the initial cycle, water saturation dropped to approximately 38% due to water production out of the core. There are some possibilities for this water production: first, it may occur due to lower density of hydrates relative to brine, resulting in volume expansion as water molecules incorporate into the hydrate structure, displacing non-bonded water. Furthermore, after hydrate dissociation, the mobile water which was immobile before being incorporated into the hydrate network, is unable to return to its original position due to changes in the capillary pressure as a result of changes in pore-size distribution [41, 42]. In addition, the significant pressure drop associated with hydrate formation, along with the CO_2 flow, further assists brine displacement toward the outlet. Notice that, greater pressure drops were observed at nucleation time during the secondary cycles (approximately 3–3.5 bars) compared to the primary cycle (1 bar), indicating a pronounced hydrate memory effect. Almost the same repetition with a greater pressure drop was observed at nucleation during secondary cycles (approximately 3–3.5 bar) compared to the primary cycle (1 bar), indicating a hydrate memory effect. This suggests that the history of hydrate formation significantly influences nucleation kinetics in subsequent cycles.

Fig. 5 presents the results from Experiment 6, conducted with a 15 wt % NaCl solution: (a) slice average water/hydrate saturations along the core length at three stages including initial brine saturation, post-hydrate growth, and brine distribution after hydrate decomposition; (b) individual X-ray images of the sand core depicting (top) two-phase

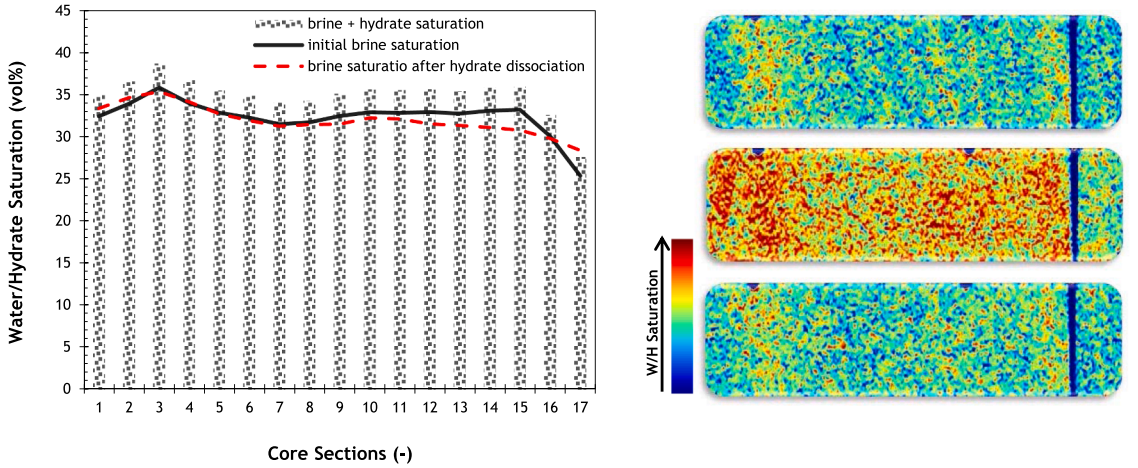

Fig. 5. (left) Slice-averaged saturations of brine/hydrate along the core length after initial brine saturation, after complete hydrate growth, and after hydrate decomposition. X-ray images of the sand core: (top) before hydrate nucleation, showing two phases—32.4 vol% brine and CO_2 gas; (middle) after hydrate growth, showing three phases—34.9 vol% brine, CO_2 hydrate, and CO_2 gas; (bottom) after hydrate dissociation.

distribution with 32.4 vol% brine and CO_2 gas before hydrate formation, (middle) three-phase distribution with 34.9 vol% brine, CO_2 hydrate, and CO_2 gas, and (bottom) the core after hydrate dissociation, showing brine and CO_2 gas. The CT images indicate a volume expansion following CO_2 hydrate formation, confirming that the density of hydrate in the core is lower than that of brine. Note that the salinity of the solution significantly influenced hydrate saturation across different experiments. Given the limited resolution of the medical CT scanner, distinguishing between water and hydrate phases in the images remains challenging. Consequently, a numerical methodology was developed in a previous study to estimate hydrate saturation for each test (M. Aghajanloo et al. [43]).

3.1. Mean ionic activity

Since hydrate nucleation predominantly occurs within the aqueous phase, gas solubility plays an important role in this process. Considering that salts influence water properties such as chemical potential and water activity which subsequently affect gas solubility, correlating hydrate saturation with mean ionic activity offers a more practical approach to describing the impact of salts on hydrate formation parameters [44,45]. This approach enables mean ionic activity to serve as a generalized parameter, capturing the effective activity of both cations and anions, and eliminates the need to specify the salt type and concentration explicitly. In this context, the mean ionic activities ($a_{i_\pm}$) of an electrolyte solution is expressed as follows [46]:

$$a_{i_\pm} = m_\pm \gamma_\pm \,, \tag{1}$$

where $\gamma_\pm$ denotes the mean ionic activity coefficient, and $m_\pm$ denotes the mean molality, defined as the geometric mean of the molalities of the individual ions in an electrolyte. The dissociation of an electrolyte into its constituent ions is governed by stoichiometric coefficients ν_+ for cations and ν_- for anions as expressed by the following relationship [47,48]:

$$m_\pm = (m_+^{\nu_+} m_-^{\nu_-})^{\frac{1}{\nu_+ + \nu_-}} \,, \tag{2}$$

where m_+ and m_- are the molalities of the cations and anions, respectively. Similarly, the mean ionic activity coefficient ($\gamma_\pm$) is defined as:

$$\gamma_\pm = (\gamma_+^{\nu_+} \gamma_-^{\nu_-})^{\frac{1}{\nu_+ + \nu_-}}, \tag{3}$$

This coefficient reflects the deviation of ions from ideal behaviour due to interionic interactions within the solution.

The mean ionic activity ($a_{i_\pm}$) can thus be defined as the product of the mean molality and the mean ionic activity coefficient. For dilute saline solution of NaCl ($m_\pm$<3) and $CaCl_2$ ($m_\pm$<1.6) the Debye–Hückel equation provides an accurate representation of the measured value of $\gamma_\pm$ (P. Debye et al., [49]; [50]):

$$\ln\gamma_\pm = \frac{-Az_+z_-I^{0.5}}{1 + BaI^{0.5}} \,, \tag{4}$$

where I is the molal basis ionic strength of the electrolyte, and A and B are numerical constants dependent on the experimental temperature and the dielectric constant of the solvent. The value of A is influenced by the relative permittivity of the solvent and temperature, while B is a function of the ion size parameter (a). The term z_- and z_+ denote the charges of the cations and anions in solution, respectively. The density of water is approximately 1 kg/L at 25°C.

However, for $m_\pm > 1.6$ (I>0.1 m) in $CaCl_2$ solutions, the higher ionic strength limits the applicability of the Debye–Hückel equation. Therefore, the Pitzer model was used, which incorporates supplementary terms to account for short-range ion-ion interactions, extending its validity to high ionic strengths (~6 mol/kg or higher) [51,52]. The mean ionic activity coefficient is calculated as follows:

$$\ln\gamma_\pm = f^\gamma + m\left(b^\gamma_{MX}\right) + m^2\left(c^\gamma_{MX}\right) \,, \tag{5}$$

Where $f^\gamma = -A_\varphi\left[\frac{I^{0.5}}{1+bI^{0.5}} + \frac{2}{b}\ln(1+bI^{0.5})\right]$ is the Debye–Hückel term, which represents long-range electrostatic interactions. Here m is the electrolyte molality, b is an empirical parameter often set to 1.2 $(\frac{kg}{mol})^{\frac{1}{2}}$, and $A_\varphi$is the Debye–Hückel slope, which is temperature dependent. For aqueous solutions at 25 °C, A_φ= 0.3915 $(\frac{kg}{mol})^{\frac{1}{2}}$ [53]. In addition, b^γ_{MX} represents the binary interaction coefficient, which quantifies short-range interactions between ions in the solution, while c^γ_{MX} is a ternary interaction coefficient, accounting for three-body interactions at very high ionic strengths.

Uncertainty in the mean ionic activity (Eq. 1) was quantified by propagating errors in the mean molality and mean activity coefficient. Because both are geometric means, calculations were performed in log-space and (Gaussian) error propagation, which treats relative errors additively and allows covariances to be included. For a single, fully dissociated binary salt prepared from one weighed solution:

$$u_r(m_\pm) = \frac{u(m_\pm)}{m_\pm} \approx u(\ln m_\pm) \tag{6}$$

Here we assume that m_+ and m_- errors are independent, therefore the covariance term is zero.

Because γ_+ and γ_- are derived from the same thermodynamic model (Debye–Hückel/Extended DH/Pitzer) at identical (I, T), their uncertainties are typically strongly correlated. Consequently, the relative standard uncertainty of the mean activity coefficient satisfies:

$$u_r(\gamma_\pm) \approx u_r(\gamma_+) \approx u_r(\gamma_-) \tag{7}$$

For mean ionic activity $a_{i_\pm} = m_\pm\gamma_\pm$, working in log-space gives $\ln a_{i_\pm} = \ln m_\pm + \ln\gamma_\pm$. If the uncertainties in $m_\pm$ and $\gamma_\pm$ can be treated as effectively independent, the relative uncertainty of mean ionic activity is obtained by adding in quadrature:

$$u_r(a_{i_\pm}) \approx \sqrt{u_r{}^2(m_\pm) \approx u_r{}^2(\gamma_\pm)} \tag{8}$$

Fig. 6 presents the variation of the mean ionic activity coefficient in the electrolyte solutions as a function of mean molality, in the range of 0–5 mol/kg, which corresponds to concentrations ranging from 0 to 25 wt% for $CaCl_2$ and 0–21 wt% for NaCl. As shown in Fig. 6, at mean molalities below 1.6 mol/kg (corresponding to concentrations below 8 wt%), $CaCl_2$ exhibits a more pronounced effect in preventing hydrate nucleation compared to NaCl at the same mean molality. However, beyond this threshold mean molality > 1.6 mol/kg, or $CaCl_2$ concentrations above 8 wt%, this trend reverses [54-56]. Although the mean ionic activity coefficients demonstrate a non-monotonic relationship with mean molality, the mean ionic activity coefficient of $CaCl_2$ solutions increases more significantly than that of NaCl solutions when the mean molality rises above ~1.1 mol/kg. This trend indicates that the hydrate inhibition efficiency of $CaCl_2$-containing solutions diminishes with increasing mean ionic activity coefficient. However, in NaCl-containing solutions, the mean ionic activity coefficient initially decreases with increasing mean molality, followed by a slight increase, after which it remains relatively constant.

To construct a unified thermodynamic pressure-temperature diagram for CO_2 hydrate, independent of salt type [34], the hydrate formation pressure is determined at temperatures ranging of −14–4°C, using the modified mean ionic activity ($a_{i_\pm}{}'$), which is defined as follows:

$$a_{i_\pm}{}' = cm\gamma_\pm \,, \tag{9}$$

where c represents the number of anions (Cl^-) in the saline solution formula. This parameter is introduced based on the rationale reported in the literature that anions can exert a stronger influence than cations in depressing hydrate equilibrium temperature, and that hydrate

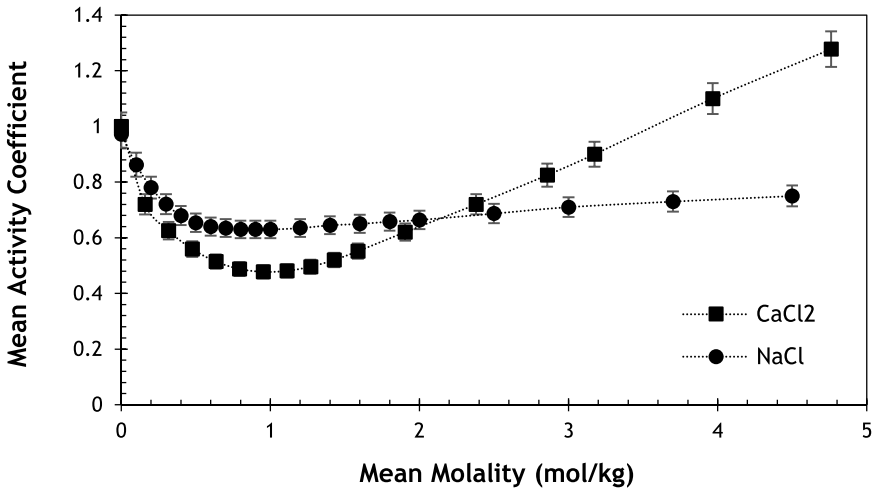

Fig. 6. Variations in the mean ionic activity coefficient as a function of mean molality for NaCl (circles) and $CaCl_2$ (squares) solution under standard conditions (25°C and 1 bar). The error bars represent the 5% deviation.

inhibition may be sensitive to anion identity and valency [27,57,54,58]. It should be noted that this ion-specific hypothesis is not explicitly isolated in the present experiments, as only chloride brines were tested. Therefore, the discussion of anion-dominant effects is based on published literature rather than on a direct ion-by-ion experimental comparison in this study. Whereas the conventional mean ionic activity ($a_i\pm$) characterizes overall electrolyte strength by combining cationic and anionic contributions, our results suggest that hydrate suppression is better captured when the anionic contribution and effective anion valency are emphasized, rather than using a single symmetric averaged activity term. To account for this reported asymmetry, we therefore employ an anion-weighted mean ionic activity ($a_i\pm'$), in which the anionic contribution receives an empirical weighting. Fig. 7 presents the equilibrium pressure lines corresponding to hydrate formation at different temperatures. The region above each line represents thermodynamic conditions under which CO_2 hydrates remain stable, meaning that hydrates will form or persist at these pressures and modified mean ionic activities. At lower temperatures (-14 to −8°C), the hydrate formation pressure remains relatively constant across different levels of modified mean ionic activity, particularly at lower values. However, at higher temperatures, the hydrate formation pressure exhibits an increasing trend with rising modified mean ionic activity.

It is important to note that this estimation is based on calculations for bulk aqueous solutions. In the case of porous media, the potential promoting or inhibiting effects of the medium should be considered.

3.2. *Induction time and mean ionic activity*

Fig. 8 presents a chart displaying the observed trends in induction time for solutions containing different concentrations of NaCl and $CaCl_2$, plotted as a function of mean ionic activity. To mitigate the potential uncertainty associated with the stochastic nature of hydrate nucleation, the average induction time across cycles was utilized. The data indicates that an increase in the mean ionic activity, corresponding to higher salt concentrations, generally leads to prolonged induction times. Furthermore, the slightly extended induction time observed at higher salinities could be attributed to a slower diffusion and dissolution rates of CO_2 at lower temperatures. The average onset of the macroscopic CO_2 hydrate nucleation for solutions with the mean ionic activity below 0.5 exhibits a slightly different trend compared to those with higher values. Notably,

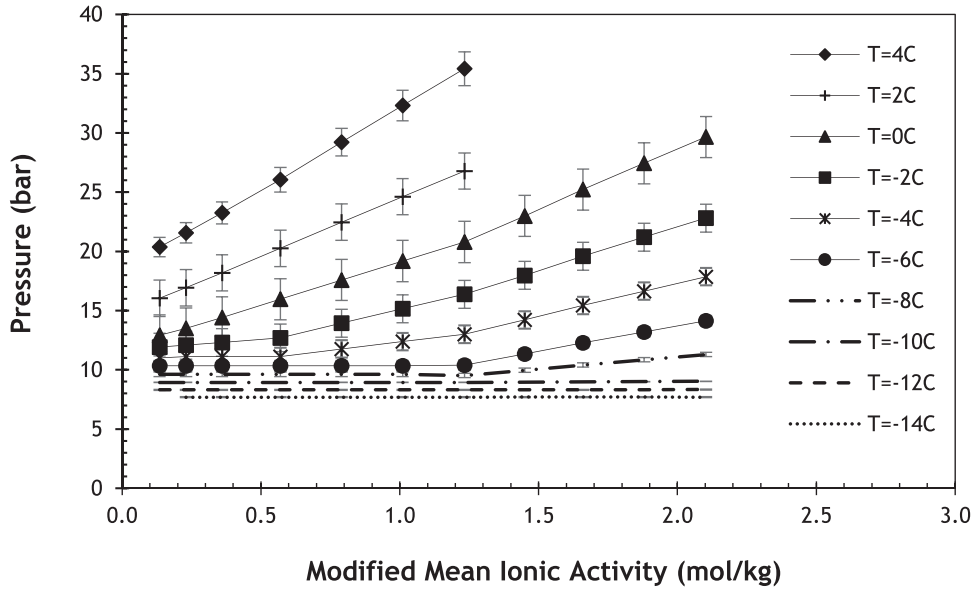

Fig. 7. CO_2 hydrate equilibrium pressure as a function of modified mean ionic activity at different temperatures. Hydrate is stable above each line at the corresponding temperature (The error bars represent the 5% deviation).

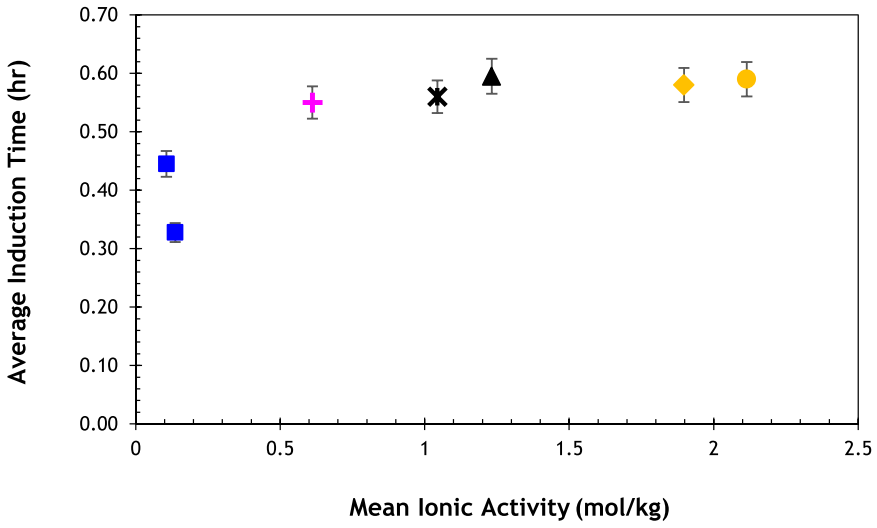

Fig. 8. Impact of mean ionic activity on average induction time of CO_2 hydrate formation (The error bar shows the uncertainty in the measurement of 5%).

the 1 wt% saline solution containing $CaCl_2$ shows a longer induction time compared to the NaCl solution. However, for solutions with the mean ionic activity exceeding 0.5, induction times remained within the range of 30 and 40 min, showing no significant variation.

Fig. 8 indicates that induction times converge at high mean ionic activities. This convergence is attributable to the pronounced depression of water activity at elevated salinities: once ionic strength surpasses a threshold, additional increases produce minimal further reduction in the availability of free water molecules and in the effective subcooling, yielding a plateau in nucleation kinetics.

3.3. Hydrate saturation change with mean ionic activity

The final hydrate saturation at the end of the growth phase has been calculated for each test based on the dynamic pressure-temperature data recorded during the test, following methodology outlined in our previous study [8]. Fig. 9 plots CO_2 hydrate saturation and the normalized hydrate saturation (hydrate saturation divided by corresponding initial water saturation) as functions of mean ionic activity across the tested electrolyte concentrations. Normalization hydrate saturation was applied because the initial water saturation varied slightly among experiments; this allows direct comparison across runs by isolating the influence of mean ionic activity on hydrate saturation, independent of differences in initial water content. This approach simplifies the analysis by emphasizing electrolyte activity rather than the specific type and concentration of the salt. According to the empirical and numerical outcomes of this study, the dotted line provides an approximate correlation between hydrate saturation and mean ionic activity.

Hydrate saturation is influenced by multiple factors, with subcooling degree and mean ionic activity of the solution being among the most critical. As shown in Fig. 6, when the mean molality exceeds 1, particularly in the presence of $CaCl_2$, the mean activity coefficient increases correspondingly. Based on this trend, it would be expected that hydrate saturation—defined as the proportion of the water volume converted into hydrate relative to the total pore volume of the porous medium—should increase with rising salinity. However, Fig. 9 reveals a different pattern, particularly at the highest mean ionic activity point corresponding to 25 wt% $CaCl_2$, where a decrease in hydrate saturation is

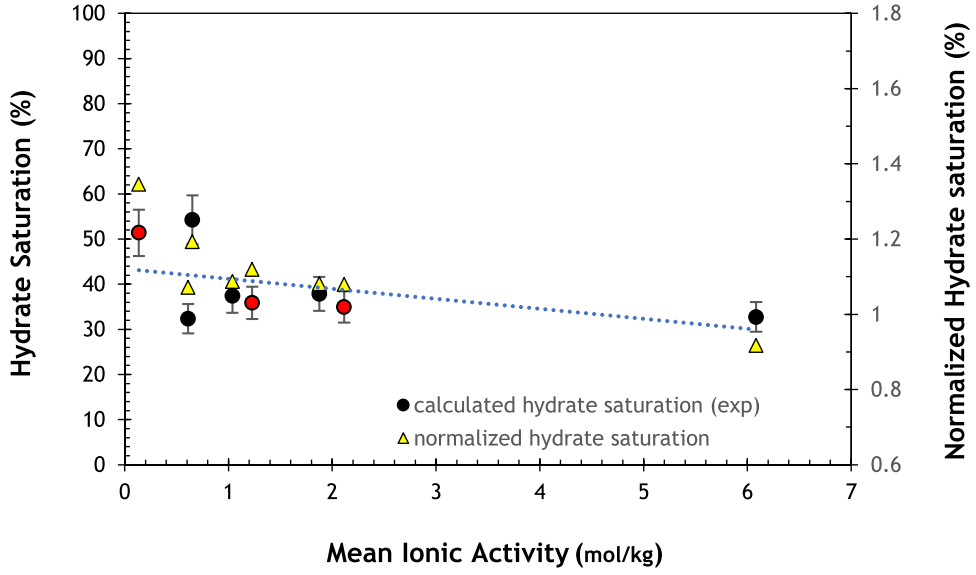

Fig. 9. The measured water saturation and the calculated hydrate saturation (black solid circles represented for $CaCl_2$ and red solid circles for NaCl) at the end of hydrate growth [59] against mean ionic activity for different salt concentrations. The dotted line shows a weak linear correlation (The error bar indicating a margin of ±5%).

observed. This deviation is likely due to an insufficient subcooling degree, which may have constrained hydrate formation despite the high ionic activity (the effective driving force for hydrate growth is reduced at higher salinities). Since salts do not integrate into the hydrate structure, a salinity gradient develops at the hydrate formation front. Moreover, as the water-to-hydrate conversion is not instantaneous, the salinity of the residual water surrounding the hydrate progressively increases throughout the nucleation process, further influencing hydrate growth dynamics. The dilution of this high-salinity solution decreases gradually until the core pores become more saturated with hydrate, leading to reduced flow patterns and further dilution requires a higher degree of diffusional character. As the surrounding water more rapidly reaches conditions outside the hydrate stability zone, it is expected that smaller hydrate cores will form in solutions with higher initial salinity. Consequently, this phenomenon can cause a non-uniform hydrate structure [12], as the composition and stability of hydrates are influenced by the properties of the surrounding fluids. This salinity increase leads to a dynamic reduction in water activity, particularly at higher salt concentrations. Additionally, higher salinity shifts the hydrate stability region towards low-temperatures/high-pressures [34]. Under these thermodynamic conditions, further hydrate formation becomes increasingly restricted due to either a diminished degree of subcooling or displacing outside the hydrate stability zone, ultimately leading to a reduced overall water-to-hydrate conversion. Since the same degree of subcooling was applied for all cases in this work, the restriction of hydrate nucleation due to insufficient subcooling is more pronounced at higher mean molality (i.e., in higher salinity solutions). In addition, differences in initial water saturation can slightly influence the final hydrate saturation, as higher water saturation generally results in greater hydrate formation.

Furthermore, salinity impacts not only the hydrate saturation but also the hydrate density and stability by influencing CO_2 solubility. As salinity increases, CO_2 dissolution decreases, reducing the amount of CO_2 encapsulated within hydrate cages and consequently lowering hydrate density. This also alters the hydration number—the ratio of water molecules to CO_2 molecules within a unit hydrate structure. Moreover, since hydrate stability strongly depends on the amount of gas captured within its lattice, this density reduction leads to a weaker and less stable hydrate framework [60,61]. For instance, as illustrated in Fig. 6, it is anticipated that the density of hydrates decreases as the mean ionic activity decreases, especially at its minimum point.

It should be noted that all experiments were conducted under a constant subcooling of 6 °C. Nevertheless, as ionic activity increases, the equilibrium temperature of CO_2 hydrate formation decreases, so that the same subcooling corresponds to a lower effective driving force for hydrate growth. At high salinities, this reduced driving force, combined with lower water activity and gas solubility, results in lower final hydrate saturation.

3.4. Hydrate saturation change with permittivity

Permittivity, also referred to as the dielectric constant, is a temperature and concentration dependent property that quantifies a material ability to attenuate an electric field. In electrolyte solutions, the presence of dissolved ions significantly influences the permittivity of the solvent. As ion concentration increases, the dielectric constant of the solvent typically diminishes [62]. This occurs because the hydration shell of solvent molecules effectively shields the ions, thereby diminishing the overall external field [63]. The empirical model for static permittivity as a function of ion concentration was introduced by Michelsen and Mollerup and is expressed as follows:

$$\varepsilon_r = \varepsilon_{S,0}\left(1 - \sum \frac{a_+ c_+}{1 + 0.160 c_+} - \sum \frac{a_- c_-}{1 + 0.160 c_-} + 0.010(c_+ + c_-)\right), \quad (10)$$

where $\varepsilon_{S,0}$ is the relative permittivity of pure saturated liquid water [64] and, a_+ and a_- are cation and anion parameters, respectively, as listed in Table 4. The concentration of cation charges is given by $c_+ = z_+ c_{cation}$ where z_+ denotes the charge number of the cation and c_{cation} is the molar concentration of the cation. Correspondingly, the concentration of anion charges is expressed as $c_- = z_- c_{anion}$, where z_- is the charge number of the anion and c_{anion} represents its molar concentration.

In gas hydrate modelling, considering the electrostatic interactions between ions inside a polar medium is essential [65]. Fig. 10 presents the correlation between hydrate saturation trends and the relative permittivity of the electrolyte solutions analysed in this study. The experimental data shows a linear trend, demonstrating that hydrate saturation rises as relative permittivity increases.

3.5. Permeability and Injectivity

The findings from our previous studies reveal that permeability and the injectivity index are influenced by CO_2 hydrate saturation [8]. Given that this study demonstrates a correlation between CO_2 hydrate saturation and salinity, it follows that permeability will also exhibit a salt-dependent behaviour [66]. This work attempts to predict permeability reduction and CO_2 injectivity impairment due to hydrate saturation in the presence of different saline solutions. Fig. 11 establishes a corresponding linear relationship between the normalized permeability and the mean ionic activity. Darcy's law was applied to calculate the normalized permeability ($\frac{k}{k_0}$) as follows:

$$\frac{k}{k_0} = \frac{\Delta P_0}{\Delta P}, \quad (11)$$

where ΔP_0 and ΔP stand for the pressure drop along the core length pre-hydrate nucleation and at the end of the hydrate growth phase, respectively.

In general, relative permeability is influenced by hydrate saturation, which in turn is impacted by water saturation level, water distribution, salinity (ionic activity), and subcooling degree among other parameters. Hydrates form within the pore spaces of the rock, effectively reducing the volume available for fluid flow. As the pore volume occupied by hydrates increases, permeability decreases because the fluid pathways become blocked, resulting in a higher differential pressure required to maintain a given flow rate. Thus, the normalized permeability reduction is also a function of the mean ionic activity.

Moreover, the water saturation level impacts the amount of water available for hydrate nucleation [8]. Higher initial water saturation provides more free water, which under favourable conditions, can increase hydrate volume (saturation) and further reduce normalized permeability. Variations in water saturation also affect the distribution of water and hydrates within the pore spaces, influencing the extent of hydrate formation and the degree of pore space blockage. This can result in a considerable decrease in permeability with the final k/k_0, potentially approaching zero.

Since the solid hydrate structure obstructs core pore spaces, leading to a reduction in permeability, any variation in hydrate saturation directly impacts permeability. In solutions with different salinities or ionic compositions, mean ionic activity influences hydrate saturation, thereby indirectly affecting relative permeability. As discussed in Section 3.1.3, an increase in mean ionic activity initially promotes higher hydrate saturation when the mean molality is below 1. However, at higher mean molality, the degree of subcooling becomes insufficient to sustain continued hydrate formation. This limitation restricts hydrate

Table 4
The parameters for NaCl and $CaCl_2$ ions.

Cation	a_+	Anion	a_-
Na^+	0.1062	Cl^-	0.1173
Ca^{2+}	0.1097		

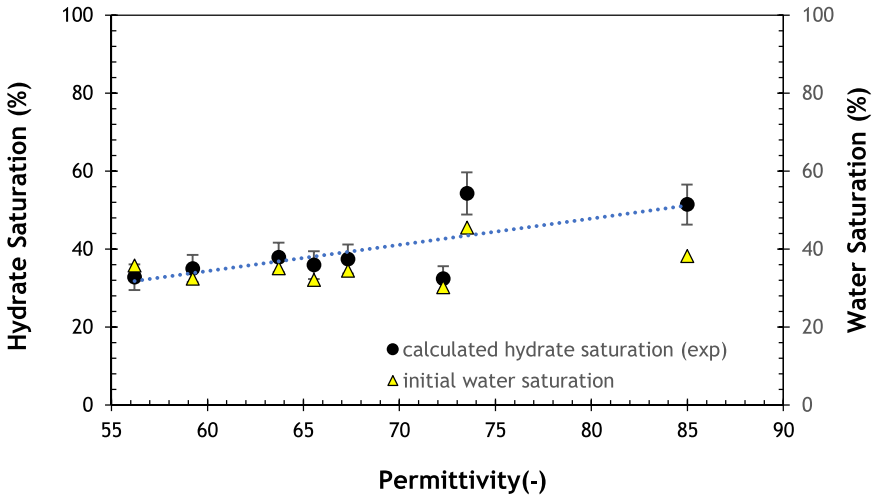

Fig. 10. The measured water saturation and the calculated final hydrate saturation over different permittivity of saline solutions. Dotted curve shows the linear correlated results (The error bar indicating a margin of ±5%).

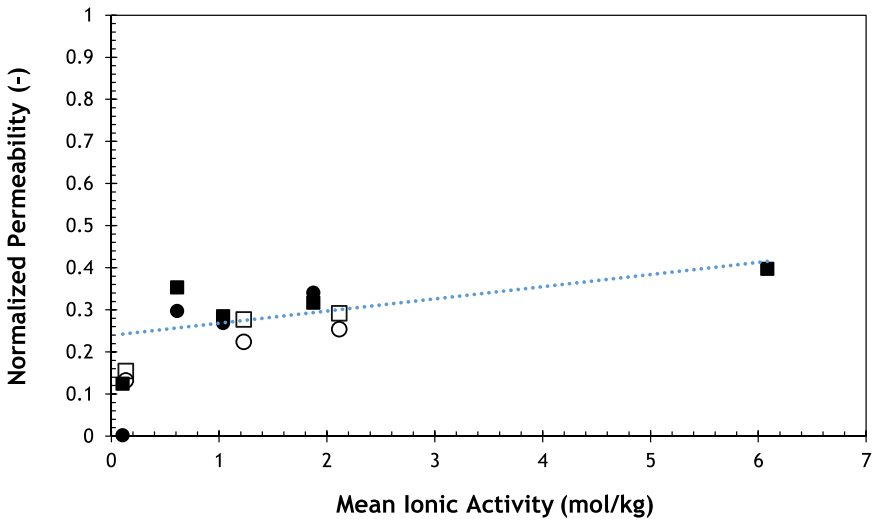

Fig. 11. Normalized permeability (k/k_0) at the end of the first and second cycles of hydrate growth as a function of mean ionic activity. Symbols represent: ■ and □: (first cycle) normalized permeability of $CaCl_2$ and NaCl solution, respectively; • and ○: (second cycle) normalized permeability of $CaCl_2$ and NaCl solution, respectively; Dotted line: corresponding function curve.

growth, resulting in lower overall hydrate saturation and a less pronounced reduction in permeability. It should be noted that, although permeability reduction is primarily correlated with hydrate saturation, the type of salt ion may also influence permeability behavior. At identical mean ionic activities, NaCl (monovalent) and $CaCl_2$ (divalent) systems can produce differences in hydrate morphology and spatial distribution within pores. Such differences may alter the extent of pore blockage and flow channelling, leading to distinct permeability responses.

Since permeability and injectivity follow a similar trend, an increase in permeability reduction corresponds to a more pronounced decline in injectivity. Therefore, based on the findings it can be inferred that, for the examined cases, the injectivity index exhibits a slight increase with increasing mean ionic activity.

4. Conclusions

CO_2 hydrates were formed in Berea sandstone saturated with NaCl or $CaCl_2$ solutions at different brine saturations. Under our experimental conditions and the assumptions made in this study, the following conclusions can be made:

- Higher initial salinity (mean molality) generally leads to a longer induction period. Nevertheless, at mean ionic activity above 0.5, while the elevated salinity of the residual water after initial hydrate nucleation is expected to suppress further hydrate nucleation, the obtained outcomes indicate that the increase in induction time is not significant.
- Hydrate saturation (S_H) is influenced by the presence of NaCl and $CaCl_2$ solutions at various concentrations, with S_H increasing with decreasing mean ionic activity of the aqueous solution.
- Salinity affects mean ionic activity, which subsequently influences hydrate saturation. Under conditions of low subcooling, an increase in mean ionic activity could result in less pronounced reductions in permeability and injectivity.

Nevertheless, this study establishes correlations among induction time, hydrate saturation, absolute permeability reduction, and their combined impact on CO_2 injectivity as a function of mean ionic activity—enabling generalized application of the results independent of

specific salt identity. However, the experiments were limited to gaseous CO_2 injection under isothermal conditions; liquid or supercritical CO_2 and two-phase (liquid–gas) flow were not considered and thus lie beyond the present scope. Future work should (i) explicitly investigate liquid and supercritical CO_2 injection to quantify how phase state modulates induction times, growth kinetics, and hydrate-plugging risk, and (ii) couple active thermal management with transient injection protocols to control near-wellbore subcooling and mitigate injectivity impairment.

CRediT authorship contribution statement

Aghajanloo Mahnaz: Writing – original draft, Software, Methodology, Investigation, Conceptualization. **S. Jones:** Writing – review & editing. **T. Zaynetdinov:** Writing – original draft. **Taghinejad S.:** Software, Investigation, Conceptualization, Data curation, Writing -Original draft preparation. **R. Farajzadeh:** Writing – review & editing, Supervision, Project administration, Methodology, Investigation, Funding acquisition, Conceptualization. **D. Voskov:** Writing – review & editing, Supervision, Project administration, Methodology, Investigation, Funding acquisition, Conceptualization.

Declaration of Competing Interest

The authors declare that they have no known competing financial interests or personal relationships that could have appeared to influence the work reported in this paper.

Acknowledgements

Authors thank Shell Global Solutions International B.V. for granting permission to publish this work. We also thank Michiel Slob for providing technical support for the study.

Data availability

Data will be made available on request.

References

[1] S.M. Benson, D.R. Cole, CO_2 Sequestration in deep sedimentary formations, Elements 4 (5) (2008) 325–331, https://doi.org/10.2113/gselements.4.5.325.
[2] K.Z. House, D.P. Schrag, C.F. Harvey, K.S. Lackner, Permanent carbon dioxide storage in deep-sea sediments, Proc. Natl. Acad. Sci. 103 (33) (2006) 12291–12295, https://doi.org/10.1073/pnas.0605318103.
[3] B. Peachey, N. Maeda, Challenging the chemistry of climate change, Chemistry 6 (6) (2024) 1439–1448. ⟨https://www.mdpi.com/2624-8549/6/6/86⟩.
[4] T. Dance, Assessment and geological characterisation of the CO2CRC Otway Project CO_2 storage demonstration site: from prefeasibility to injection, Mar. Pet. Geol. 46 (2013) 251–269, https://doi.org/10.1016/j.marpetgeo.2013.06.008.
[5] C.M. Oldenburg, S.M. Benson, CO_2 injection for enhanced gas production and carbon sequestration, SPE Int. Pet. Conf. Exhib. Mex. (2002).
[6] Y. Pamukcu, S. Hurter, L. Jammes, D. Vu-Hoang, L. Pekot, Characterizing and predicting short term performance for the In Salah Krechba field CCS joint industry project, Energy Procedia 4 (2011) 3371–3378.
[7] J. Underschultz, C. Boreham, T. Dance, L. Stalker, B. Freifeld, D. Kirste, J. Ennis-King, CO_2 storage in a depleted gas field: an overview of the CO2CRC otway project and initial results, Int. J. Greenh. Gas. Control 5 (4) (2011) 922–932.
[8] M. Aghajanloo, S. Jones, L. Yan, D. Voskov, R. Farajzadeh, Evaluation of CO_2 hydrate saturation in porous core experiments using medical CT images, Energy & Fuels 38 (12) (2024) 11037–11042, https://doi.org/10.1021/acs.energyfuels.4c01537.
[9] C.M. Oldenburg, Screening and ranking framework for geologic CO_2 storage site selection on the basis of health, safety, and environmental risk, Environ. Geol. 54 (2008) 1687–1694.
[10] A. Hosseini Zadeh, I. Kim, S. Kim, Characteristics of formation and dissociation of CO2 hydrates at different CO2-Water ratios in a bulk condition, J. Pet. Sci. Eng. 196 (2021) 108027, https://doi.org/10.1016/j.petrol.2020.108027.
[11] J. Sun, X. Hao, C. Li, N. Wu, Q. Chen, C. Liu, Y. Li, Q. Meng, L. Huang, Q. Bu, Experimental study on the distribution characteristics of CO2 in methane hydrate-bearing sediment during CH_4/CO_2 replacement, Energies 15 (15) (2022) 5634. ⟨https://www.mdpi.com/1996-1073/15/15/5634⟩.
[12] J. Husebø, G. Ersland, A. Graue, B. Kvamme, Effects of salinity on hydrate stability and implications for storage of CO2 in natural gas hydrate reservoirs, Energy Procedia 1 (1) (2009) 3731–3738, https://doi.org/10.1016/j.egypro.2009.02.172.
[13] N. Li, Z. Fan, H. Ma, S. Jia, J. Kan, C. Sun, S. Liu, Permeability of hydrate-bearing sediment formed from CO2-N2 mixture, J. Mar. Sci. Eng. 11 (2) (2023) 376. ⟨https://www.mdpi.com/2077-1312/11/2/376⟩.
[14] S. Lee, Y. Seo, Experimental measurement and thermodynamic modeling of the mixed CH4 + C3H8 clathrate hydrate equilibria in silica gel pores: effects of pore size and salinity, Langmuir 26 (12) (2010) 9742–9748, https://doi.org/10.1021/la100466s.
[15] L. Wang, M. Dou, Y. Wang, Y. Xu, Y. Li, Y. Chen, L. Li, A review of the effect of porous media on gas hydrate formation, ACS Omega 7 (38) (2022) 33666–33679, https://doi.org/10.1021/acsomega.2c03048.
[16] A. Zeinijahromi, H. Al-Jassasi, S. Begg, P. Bedrikovetski, Improving sweep efficiency of edge-water drive reservoirs using induced formation damage, J. Pet. Sci. Eng. 130 (2015) 123–129, https://doi.org/10.1016/j.petrol.2015.04.008.
[17] E.D. Sloan Jr, C.A. Koh, Clathrate hydrates of natural gases, CRC press, 2007.
[18] K. Nagashima, S. Orihashi, Y. Yamamoto, M. Takahashi, Encapsulation of saline solution by tetrahydrofuran clathrate hydrates and inclusion migration by recrystallization, J. Phys. Chem. B 109 (20) (2005) 10147–10153, https://doi.org/10.1021/jp040680i.
[19] B. Sowa, X.H. Zhang, P.G. Hartley, D.E. Dunstan, K.A. Kozielski, N. Maeda, Formation of ice, tetrahydrofuran hydrate, and methane/propane mixed gas hydrates in strong monovalent salt solutions, Energy & Fuels 28 (11) (2014) 6877–6888, https://doi.org/10.1021/ef501701y.
[20] P. Dehghani, A. Sinquin, N. Gland, A.M. Tang, A. Estublier, Investigating cyclopentane hydrate nucleation and growth using microfluidics, Sci. Tech. Energ. Transit. 78 (2023) 36, https://doi.org/10.2516/stet/2023034.
[21] S.H.B. Yang, P. Babu, S.F.S. Chua, P. Linga, Carbon dioxide hydrate kinetics in porous media with and without salts, Appl. Energy 162 (2016) 1131–1140, https://doi.org/10.1016/j.apenergy.2014.11.052.
[22] Y. Li, M. Chen, H. Song, P. Yuan, D. Liu, B. Zhang, H. Bu, Methane hydrate formation in the stacking of kaolinite particles with different surface contacts as nanoreactors: a molecular dynamics simulation study, Appl. Clay Sci. 186 (2020) 105439, https://doi.org/10.1016/j.clay.2020.105439.
[23] H. Ghaedi, M. Ayoub, S. Sufian, G. Murshid, S. Farrukh, A.M. Shariff, Investigation of various process parameters on the solubility of carbon dioxide in phosphonium-based deep eutectic solvents and their aqueous mixtures: Experimental and modeling, Int. J. Greenh. Gas Control 66 (2017) 147–158, https://doi.org/10.1016/j.ijggc.2017.09.020.
[24] Z. Duan, R. Sun, An improved model calculating CO_2 solubility in pure water and aqueous NaCl solutions from 273 to 533 K and from 0 to 2000 bar, Chem. Geol. 193 (3-4) (2003) 257–271.
[25] R.B. Lamorena, W. Lee, Formation of carbon dioxide hydrate in soil and soil mineral suspensions with electrolytes, Environ. Sci. & Technol. 42 (8) (2008) 2753–2759, https://doi.org/10.1021/es702179p.
[26] T. Svartaas, M. Kelland, L. Dybvik, Experiments related to the performance of gas hydrate kinetic inhibitors, Ann. N. Y. Acad. Sci. 912 (1) (2000) 744–752.
[27] H. Lu, R. Matsumoto, Y. Tsuji, H. Oda, Anion plays a more important role than cation in affecting gas hydrate stability in electrolyte solution? — a recognition from experimental results, Fluid Phase Equilibria 178 (1) (2001) 225–232, https://doi.org/10.1016/S0378-3812(00)00464-7.
[28] L. Geng, J. Cai, C. Lu, X. Qin, R. Qi, F. Meng, Y. Xie, Z. Sha, X. Wang, C. Sun, Phase equilibria of natural gas hydrates in bulk brine and marine sediments from the South China Sea, J. Chem. & Eng. Data 66 (11) (2021) 4064–4074, https://doi.org/10.1021/acs.jced.1c00307.
[29] H. Ye, J. Chen, Y. Yao, P. Dong, D. Chen, M. Niu, J. Duan, X. Wu, D. Li, Y. Jiang, M. Zi, How injecting CO2 enhances marine natural gas hydrate exploitation: review and prospect, Renew. Sustain. Energy Rev. 222 (2025) 116011, https://doi.org/10.1016/j.rser.2025.116011.
[30] S. Almenningen, E. Iden, M.A. Fernø, G. Ersland, Salinity effects on pore-scale methane gas hydrate dissociation, J. Geophys. Res. Solid Earth 123 (7) (2018) 5599–5608, https://doi.org/10.1029/2017JB015345.
[31] A.A. Eftekhari, R. Farajzadeh, Effect of foam on liquid phase mobility in porous media, Sci. Rep. 7 (1) (2017) 43870, https://doi.org/10.1038/srep43870.
[32] L. Klinkenberg, The permeability of porous media to liquids and gases, Drill. Prod. Pract. (2012) 200–213.
[33] A. Verruijt, Darcy's Law, in: A. Verruijt (Ed.), Theory of Groundwater Flow, Macmillan Education UK, 1970, pp. 6–13, https://doi.org/10.1007/978-1-349-00175-0_2.
[34] E. Andres-Garcia, A. Dikhtiarenko, F. Fauth, J. Silvestre-Albero, E.V. Ramos-Fernández, J. Gascon, A. Corma, F. Kapteijn, Methane hydrates: nucleation in microporous materials, Chem. Eng. J. 360 (2019) 569–576.
[35] L. Chen, C.-Y. Sun, G.-J. Chen, Y.-Q. Nie, Thermodynamics model of predicting gas hydrate in porous media based on reaction−adsorption two-step formation mechanism, IND. & ENG. CHEM. RES. IND ENG CHEM RES 49 (2010), https://doi.org/10.1021/ie901878p.
[36] S.A. Bagherzadeh, I.L. Moudrakovski, J.A. Ripmeester, P. Englezos, Magnetic resonance imaging of gas hydrate formation in a bed of silica sand particles, Energy & Fuels 25 (7) (2011) 3083–3092, https://doi.org/10.1021/ef200399a.
[37] S.B. Cha, H. Ouar, T.R. Wildeman, E.D. Sloan, A third-surface effect on hydrate formation, J. Phys. Chem. 92 (23) (1988) 6492–6494, https://doi.org/10.1021/j100334a006.
[38] Y. Qin, L. Shang, Z. Lv, J. He, X. Yang, Z. Zhang, Methane hydrate formation in porous media: overview and perspectives, J. Energy Chem. 74 (2022) 454–480, https://doi.org/10.1016/j.jechem.2022.07.019.

[39] A.S. Stoporev, A.P. Semenov, V.I. Medvedev, B.I. Kidyarov, A.Y. Manakov, V. A. Vinokurov, Nucleation of gas hydrates in multiphase systems with several types of interfaces, J. Therm. Anal. Calorim. 134 (1) (2018) 783–795, https://doi.org/10.1007/s10973-018-7352-2.
[40] S. Fan, L. Yang, X. Lang, Y. Wang, D. Xie, Kinetics and thermal analysis of methane hydrate formation in aluminum foam, Chem. Eng. Sci. 82 (2012) 185–193, https://doi.org/10.1016/j.ces.2012.07.040.
[41] J. Wang, L. Zhang, K. Ge, H. Dong, Capillary pressure in the anisotropy of sediments with hydrate formation, Fuel 289 (2021) 119938, https://doi.org/10.1016/j.fuel.2020.119938.
[42] S.-T. Zhang, L.-L. Wang, Pore pressure built-up in hydrate-bearing sediments during phase transition: a poromechanical approach, Pet. Sci. 20 (1) (2023) 482–494, https://doi.org/10.1016/j.petsci.2022.08.009.
[43] M. Aghajanloo, L. Yan, S. Berg, D. Voskov, R. Farajzadeh, Impact of CO_2 hydrates on injectivity during CO_2 storage in depleted gas fields: a literature review, Gas. Sci. Eng. 123 (2024) 205250, https://doi.org/10.1016/j.jgsce.2024.205250.
[44] R.R. Ratnakar, A. Venkatraman, A. Kalra, B. Dindoruk, On the prediction of gas solubility in brine solutions with single or mixed salts: applications to gas injection and CO2 capture/sequestration, J. Nat. Gas. Sci. Eng. 81 (2020) 103450, https://doi.org/10.1016/j.jngse.2020.103450.
[45] H. Sørensen, K.S. Pedersen, P.L. Christensen, Modeling of gas solubility in brine, Org. Geochem. 33 (6) (2002) 635–642, https://doi.org/10.1016/S0146-6380(02)00022-0.
[46] G.N. Lewis, M. Randall, K.S. Pitzer, L. Brewer, Thermodynamics, Dover Publications, 2020. ⟨https://books.google.nl/books?id=E04qygEACAAJ⟩.
[47] P.W. Atkins, J. de Paula, Atkins' physical chemistry, OUP Oxford, 2014. ⟨https://books.google.nl/books?id=sWTYAwAAQBAJ⟩.
[48] R.A. Robinson, R.H. Stokes, Electrolyte solutions: second revised edition, Dover Publications, Incorporated, 2012. ⟨https://books.google.nl/books?id=6ZVkqm-J9GkC⟩.
[49] P. Debye, a. E. H, Zur Theorie der Elektrolyte. I. Gefrierpunktserniedrigung und verwandte Erscheinungen, Phys. Z. 24 (1923) 305.
[50] M.R. Wright, An introduction to aqueous electrolyte solutions, Wiley, 2007. ⟨https://books.google.nl/books?id=dK-HJCErvFEC⟩.
[51] K.S. Pitzer, Thermodynamics of electrolytes. I. Theoretical basis and general equations, J. Phys. Chem. 77 (2) (1973) 268–277, https://doi.org/10.1021/j100621a026.
[52] K.S. Pitzer. Activity Coefficients in Electrolyte Solutions, 2nd ed.)., CRC Press, 1991 https://doi.org/10.1201/9781351069472.
[53] T.Z. Fahidy, Activity coefficients in electrolyte solutions (second edition), edited by Kenneth S. Pitzer, 1991, 542 + vi pages, CRC Press, Boca Raton, FL; ISBN 0-8493-5415-3. Price: US$ 195.00, Can. J. Chem. Eng. 71 (3) (1993) 494, https://doi.org/10.1002/cjce.5450710328.
[54] E. Rodil, J.H. Vera, Individual activity coefficients of chloride ions in aqueous solutions of MgCl2, CaCl2 and BaCl2 at 298.2 K, Fluid Phase Equilibria 187-188 (2001) 15–27, https://doi.org/10.1016/S0378-3812(01)00523-4.
[55] I.Y. Shilov, A.K. Lyashchenko, Anion-specific effects on activity coefficients in aqueous solutions of sodium salts: modeling with the extended Debye–Hückel theory, J. Solut. Chem. 48 (2) (2019) 234–247, https://doi.org/10.1007/s10953-019-00860-8.
[56] T. Yamaguchi, T. Matsuoka, S. Koda, A theoretical study on the frequency-dependent electric conductivity of electrolyte solutions, J. Chem. Phys. 127 (23) (2007) 234501.
[57] Q. Lv, X. Zang, X. Li, G. Li, Effect of seawater ions on cyclopentane-methane hydrate phase equilibrium, Fluid Phase Equilibria 458 (2018) 272–277.
[58] Y. Zhou, Z. Chen, N. Maeda, H. Li, Effect of ion specificity on thermodynamic inhibition of CH4 and CO_2 hydrates: an experimental and modeling study, Fluid Phase Equilibria 589 (2025) 114256, https://doi.org/10.1016/j.fluid.2024.114256.
[59] M. Aghajanloo, S.M. Taghinejad, D. Voskov, R. Farajzadeh, Influence of water saturation and water memory on CO_2 hydrate formation/dissociation in porous media under flowing condition, Chem. Eng. J. 492 (2024) 152455, https://doi.org/10.1016/j.cej.2024.152455.
[60] A. Hachikubo, M. Kida, D. Yahagi, G. Fuseya, S. Takeya, Effect of temperature and pressure on the hydration number of methane hydrate, Energy & Fuels 38 (11) (2024) 9676–9682, https://doi.org/10.1021/acs.energyfuels.4c01124.
[61] Y. Seo, H. Lee, B.-J. Ryu, Hydration number and two-phase equilibria of CH4 hydrate in the deep ocean sediments, Geophys. Res. Lett. 29 (8) (2002) 85-81–85-84, https://doi.org/10.1029/2001GL014226.
[62] M.L. Michelsen, J.M. Mollerup, Thermodynamic models: fundamentals & computational aspects, Tie-Line Publications, 2007. ⟨https://books.google.nl/books?id=qjmeOgAACAAJ⟩.
[63] T. Luo, Gas hydrate conditions prediction in the presence of salts by considering modified relative permittivity of solution; application of the Kirkwood-Onsager approach, Chem. Eng. Sci. 304 (2025) 121060, https://doi.org/10.1016/j.ces.2024.121060.
[64] D.P. Fernández, A.R.H. Goodwin, E.W. Lemmon, J.M.H. Levelt Sengers, R. C. Williams, A formulation for the static permittivity of water and steam at temperatures from 238 K to 873 K at pressures up to 1200 MPa, including derivatives and Debye–Hückel coefficients, J. Phys. Chem. Ref. Data 26 (4) (1997) 1125–1166, https://doi.org/10.1063/1.555997.
[65] B. Maribo-Mogensen, G.M. Kontogeorgis, K. Thomsen, Modeling of dielectric properties of aqueous salt solutions with an equation of state, J. Phys. Chem. B 117 (36) (2013) 10523–10533, https://doi.org/10.1021/jp403375t.
[66] J.R. Castaneda, S. Kahrobaei, M. Aghajanloo, D. Voskov, R. Farajzadeh, Numerical and experimental investigation of impact of CO_2 hydrates on rock permeability, Fuel 381 (2025) 133708, https://doi.org/10.1016/j.fuel.2024.133708.